Journal of
Intelligent Material
Systems and Structures

Original Article

Journal of Intelligent Material Systems and Structures
2023, Vol. 34(14) 1702–1712

DOI: 10.1177/1045389X231151249
journals.sagepub.com/home/jim
SAGE

Analysis of electret-based vibration energy harvesting devices with curved-beam hinges

Dooyoung Hah

Abstract

Recently, vibration energy harvesting devices have gained growing interests. One of the main requirements for them is a broad bandwidth owing to stochastic spectral characteristics of the general vibration sources. Among various approaches for wide bandwidth, curved-beam hinges are quite attractive due to their simple structures. Although there have been several reports on curved beams, a more detailed study is needed. The device under study is an electret-based one with balanced comb-drive configuration. The whole system is modeled by using nonlinear stochastic differential equations. The numerical analysis results show that there is an optimum curve height for maximum power output, which depends on various conditions, such as external vibration strength, comb-drive dimensions, and initial electret charges. At the external acceleration magnitude of 0.02*g* and 0.05*g*, the device with curved beams can produce up to 2.9 times and 4.8 times higher power output, respectively, than one with straight beams for given device geometries. To the contrary, at lower and higher vibration magnitudes, straight-beam devices harvest more energy than curved-beam ones. Therefore, it can be concluded that the curved beam height needs to be carefully determined based on the conditions of the application, especially on the characteristics of the external vibration sources.

Keywords

Energy harvester, mechanical vibration, nonlinear spring, curved beam, electret

Introduction

Energy harvesting has gained substantial interests lately in various fields, and its momentum has been growing in the context of sustainable development. In most of the energy harvesting application areas such as internet of things (IoTs), wireless sensor networks (WSNs), and implantable medical devices (IMDs), the main rationales either for complete replacement or for supplementation of conventional batteries stem from their issues in size, lifetime, and complication associated with replacement tasks. In the case of IMDs, especially, surgical operations are often needed for battery replacement. Various energy sources have been explored, including solar radiation, wind, water stream, tidal waves, temperature gradient, electromagnetic waves, acoustic noise, human motion, vibration, and so on. Vibration energy sources are particularly interesting among them for their ubiquitous presence as Roundy et al. (2003) reported. The report also includes a number of vibration sources in our surroundings as well as their average strengths and frequency characteristics.

Energy efficiency is one of the most important performance indicators in vibration energy harvesting (VEH) devices. The main research efforts in this regard can be divided into three directions: (1) maximization of coupling from ambient vibration to mechanical energy of the harvesting devices, (2) optimization of transduction from the mechanical energy to the electrical energy within the harvesters, and (3) efficiency improvement in conversion from alternating current (ac) to direct current (dc). Sometimes, those directions need to be pursued together due to their interrelations. In the current study, the first two aspects are examined together, with the main focus on the mechanical structure of the electrostatic VEH devices.

Many research groups have paid close attention to the frequency response of the mechanical structures of the harvesting devices. When a vibration energy source

Department of Electrical and Electronics Engineering, Abdullah Gül University, Kayseri, Türkiye

Corresponding author:
Dooyoung Hah, Department of Electrical and Electronics Engineering, Abdullah Gül University, Sumer Kampusu, Barbaros Mah., Kayseri 38030, Türkiye.
Email: dooyoung.hah@agu.edu.tr

has a well-defined, seldom-drifting peak frequency with narrow bandwidth, one can design a mechanical structure to have the matching resonant frequency with high quality factor. However, more often than not, the vibration energy sources are found to bear broadband, non-harmonic spectral characteristics, which can be described as colored noise. Consequently, a number of researchers have been working on energy harvesters with broadband frequency responses to match with those source characteristics.

Various approaches have been attempted so far in order to achieve broadband frequency responses in VEHs. Several groups explored Duffing oscillators based on a cantilever beam positioned in the middle of two magnets or on a similar configuration (Cottone et al., 2009; Erturk et al., 2009; Ferrari et al., 2011; Litak et al., 2010; Pereira et al., 2019; Sebald et al., 2011). Although broadband frequency responses have been obtained with those configurations, it is difficult to miniaturize this type of device, which becomes a bottleneck for applications with limited footprints. Other groups examined an array of single degree-of-freedom (SDOF) structures, each of which has a different resonant frequency (Xiao et al., 2014; Xue et al., 2008). This approach realizes broadband response by superposing those individual spectra. However, since only one or a few of the SDOF structures are active at a certain time, its power density becomes significantly low. Another approach has been to adopt multi-degree-of-freedom (MDOF) structures, where structures with different resonant frequencies are mechanically coupled together (Jang et al., 2011; Kim et al., 2011; Li et al., 2019; Tang and Yang, 2012; Upadrashta and Yang, 2018; Wu et al., 2013). This approach also has a challenge in terms of miniaturization. Yet, there is another approach, which is to utilize spring nonlinearity.

Most of the nonlinear springs for energy harvesting applications that have been examined so far, bear the basic structure of a clamped-clamped beam. It is a well-known fact that a clamped–clamped beam (even a straight one) exhibits nonlinear spring characteristics (Senturia, 2007). When a clamped–clamped beam is deformed, the deformation behavior includes both bending and stretching of the beam. While bending is responsible for the linear relationship (between the force and the displacement) of the spring, nonlinearity comes from the stretching. The linear spring property dominates at small displacement. As deformation increases, however, nonlinearity becomes more remarkable. As a rule of thumb, the nonlinear component becomes more dominant as the beam center displacement exceeds the beam width (dimension in the direction of deformation). Due to this nonlinearity, a clamped–clamped beam is also called an amplitude-stiffened Duffing spring. Hajati and Kim (2011) built and tested a piezoelectric energy harvesting device by using a straight clamped–clamped beam, and observed broadband spectral characteristics under harmonic excitation.

When an initial curve is added to a clamped–clamped beam, this makes the spring a Duffing–Holmes oscillator, which contains both of the second (quadratic) and the third (cubic) order nonlinearities. It is well known that a Duffing–Holmes oscillator can exhibit bistability. To the contrary, a straight clamped–clamped beam only contains the third order nonlinearity, and therefore, is without bistability. There are two possible ways to make an initial curve to a beam. Some groups applied axial pressure to buckle beams (Ando et al., 2014; Cottone et al., 2012; Eltanany et al., 2017; Liu et al., 2016; Van Blarigan et al., 2012; Zhu and Zu, 2013). This configuration has an advantage of axial symmetry. However, it is not advantageous when it comes to miniaturization of the device. Other groups designed the original beams to have curve shapes initially (Ando et al., 2012; Du et al., 2018; Nguyen et al., 2013; Nguyen and Halvorsen, 2011; Scerri, 2015). This structure, also called pre-buckled or pre-shaped beams, is much more advantageous in terms of miniaturization. The current study aims to examine this (pre-shaped) curved beam as a spring in electrostatic VEH devices.

An electrostatic method is one of the three main transduction mechanisms used in vibration energy harvesting, other two being piezoelectric and electromagnetic methods. The electrostatic mechanism has an advantage in terms of integration with the electronics (hence in terms of miniaturization). Electrostatic transduction is also advantageous at a small scale with higher power density. Various configurations have been examined, including a rotation type (Boland et al., 2003), a parallel-plate type (Torres and Rincon-Mora, 2006; Zhang et al., 2018), and a comb-drive type (Fu and Suzuki, 2014; Hagiwara et al. 2012; Honma et al., 2018, 2019; Meninger et al., 1999; Nguyen et al., 2013; Sterken et al., 2003). The comb-drive type is particularly interesting due to its relatively wide motion range. This type of VEH was introduced by Meninger et al. (1999). Early comb-drive VEH devices did not utilize electrets, and the timing of the associated switches was controlled by accompanying circuits. Sterken et al. (2003) proposed addition of electrets to the VEH devices, in a form of an electret wafer bonded to a comb-drive wafer, to simplify the control circuit, and hence, to improve the power conversion efficiency. Comb-drive VEHs reported by Hagiwara et al. (2012) embedded electrets directly within the combs by charging the electret film on the sidewalls of the fingers via soft X-ray. Electret-less comb-drive VEHs by Nguyen et al. (2013) employed curved beams, and demonstrated broad bandwidth characteristics. One of the aspects considered in VEH design has been in relation to the strength of the vibration. Fu and Suzuki (2014) presented a VEH that combines an area-changing mode

and a gap-changing mode, aiming to cover a wide range of vibration strengths. VEHs reported by Honma et al. (2018, 2019) feature a balanced comb-drive configuration, aiming at improved conversion efficiency at low vibration strengths. It is also noteworthy that in their work, the formation of electrets was realized by polarizing doped oxides on the sides of the fingers.

This paper presents the numerical analysis of electret-based comb-drive VEHs with curved-beam hinges (Hah, 2021). The main aim of the study is to examine the effect of curved beam heights to the harvested energy, especially at different external vibration strengths. As the input vibration, colored noise is considered. General ambient vibration sources have random characteristics. Consequently, response to the random vibrations, in other words, colored-noise response is more important in the practical applications. Nevertheless, most of the reports so far provided the results tested with harmonic vibrations. There have been only a handful of groups who reported the performances of the energy harvesting devices with random excitation (Ando et al., 2012; Cottone et al., 2012; De Paula et al., 2015; Dhote et al., 2019; Litak et al., 2010; Nguyen et al., 2013; Pereira et al., 2019; Zhao and Erturk, 2012). Among them, just a few groups' devices (Ando et al., 2012; Cottone et al. 2012; Nguyen et al., 2013) featured curved-beam hinges. Therefore, more in-depth study—such as optimum curved beam dimensions and their relationships to the source strength—is necessary, which is the main subject of the current paper. Colored-noise response of the electret-based comb-drive VEHs with curved-beam hinges will be examined via numerical analysis by using stochastic differential equations (SDE). Section "Methods" will describe the analysis method in details, and the results will be presented in Section "Results."

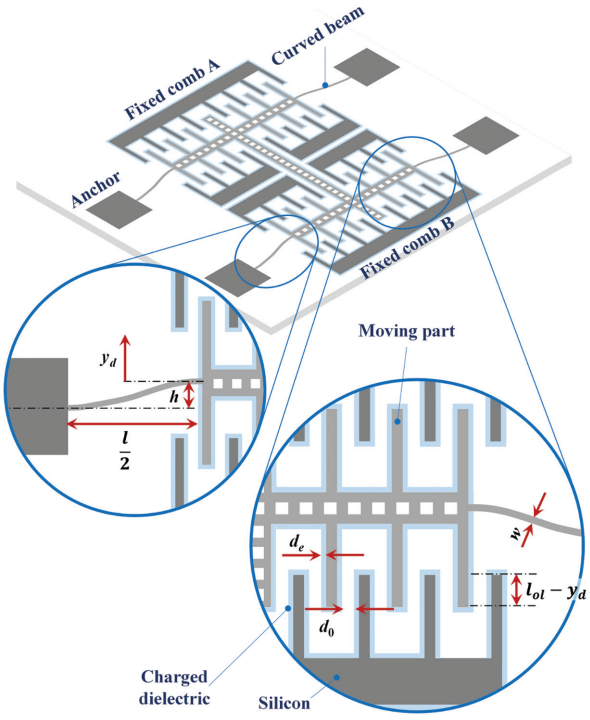

Figure 1. Conceptual illustration of an electret-based vibration energy harvesting device with curved beam hinges. For simplicity, a proof mass is omitted in the sketch. *T*: thickness of the structure in the out-of-plane direction.

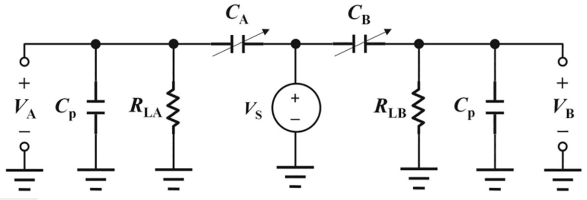

Figure 2. Equivalent circuit including electrets, comb-drives (C_A & C_B), loads (R_{LA} & R_{LB}), and parasitic capacitances (C_p).

Methods

Figure 1 illustrates a conceptual sketch of an electret-based VEH with curved beam hinges. The device configuration, more or less, follows that of Honma et al. (2018, 2019). A proof mass (m) is to be placed on top of the moving part, but omitted in the sketch. Two sets of comb-drives (finger gap: d_0; original finger overlap: l_{ol}) are employed in a balanced manner, each of which is connected to the corresponding load. Electrets are embedded within the comb-drives, and formed by charging the dielectrics (width: d_e; dielectric constant: ε_e) on the sidewalls of the fingers. As the mass moves in response to the external vibration, the comb fingers also move, inducing charge redistribution in the electrets. This charge redistribution contributes to the electric power generation. One of the critical design parameters of the device is the curved-beam height (denoted as h in Fig. 1). The spring nonlinearity is highly dependent on the beam height, and hence, it becomes the main design parameter. As h reaches a certain height, the curved beam starts to exhibit bistability. The critical height (h_{cr}) where the bistability starts to appear can be derived to be (Qiu et al., 2004),

$$h_{cr} = \frac{4\sqrt{3}}{3} w, \tag{1}$$

where w is the width of the beam. With the w value of 20 μm, h_{cr} becomes 46.2 μm. Throughout this paper, the beam height will be expressed with a unit of h_{cr}. y_d indicates the displacement of the moving part, and it is assumed that the external acceleration (a_{ext}) is exerted in the direction of y_d.

Figure 2 depicts the equivalent circuit of the electrical part of the VEH and the load. The equivalent

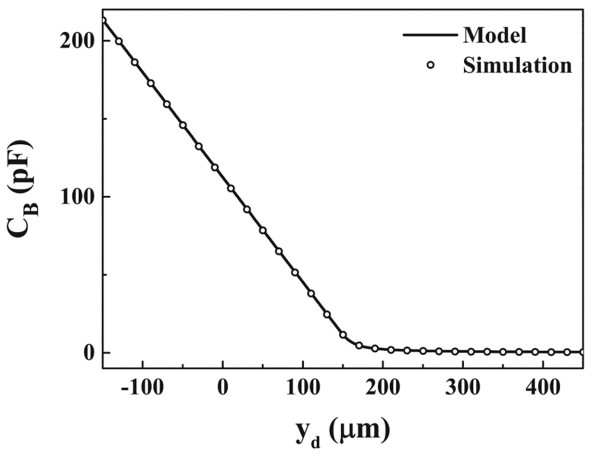

Figure 3. Calculated capacitance of the comb-drive B with respect to the displacement (y_d) of the moving part. Line: calculation via (5). Symbol: simulation via COMSOL Multiphysics®. Device geometries are given in Table 1. C_f: 16 pF/m, a_0: 0.5653 pF/m, a_1: 10.81 pF/m, a_2: 4.612 pF/m, b_1: 13.55 μm, b_2: 72.27 μm.

circuit is based on the model by Yang et al. (2019), who described the dynamic state of the electret-based VEH as the rearrangement of charges to reach a dynamic electrical equilibrium in response to the electric field change, induced by the movement of the electrode. Although the VEH in Yang et al. (2019) is in a different type from that of the current work (i.e., a parallel-plate type vs a comb-drive type), the model can be applied to the current device based on the same principle. In the equivalent circuit, V_S is the voltage associated with the initial charge on the electret, that is, surface potential, and modeled as the external voltage source. C_A and C_B are the variable capacitances of the comb-drive A and B, respectively. R_{LA} and R_{LB} are the loads, and C_p is the parasitic capacitance. V_A and V_B are defined as the voltages on the loads. The following equations can be established from the circuit:

$$\frac{V_A}{R_{LA}} + \left(C_A + C_p\right)\frac{dV_A}{dt} - \left(V_S - V_A\right)\frac{dC_A}{dt} = 0 \qquad (2)$$

$$\frac{V_B}{R_{LB}} + \left(C_B + C_p\right)\frac{dV_B}{dt} - \left(V_S - V_B\right)\frac{dC_B}{dt} = 0 \qquad (3)$$

C_A and C_B vary according to the displacement (y_d). Figure 3 (symbol) shows C_B with respect to y_d when l_{ol} is 150 μm, calculated by using COMSOL Multiphysics®. In order to reflect the variable capacitance values more accurately in the analysis, the following fitting equations were used:

$$C_A(y_d) = \begin{cases} 2N_f T\left[\frac{\varepsilon_0(l_{ol}+y_d)}{d_0+2\frac{d_e}{\varepsilon_e}} + C_f\right], & y_d \geqslant -l_{ol} \\ 2N_f T\left[a_0 + a_1\exp\left(\frac{l_{ol}+y_d}{b_1}\right) + a_2\exp\left(\frac{l_{ol}+y_d}{b_2}\right)\right], & y_d < -l_{ol} \end{cases} \qquad (4)$$

$$C_B(y_d) = \begin{cases} 2N_f T\left[\frac{\varepsilon_0(l_{ol}-y_d)}{d_0+2\frac{d_e}{\varepsilon_e}} + C_f\right], & y_d \leqslant l_{ol} \\ 2N_f T\left[a_0 + a_1\exp\left(\frac{l_{ol}-y_d}{b_1}\right) + a_2\exp\left(\frac{l_{ol}-y_d}{b_2}\right)\right], & y_d > l_{ol} \end{cases} \qquad (5)$$

where N_f and ε_0 are the number of fingers and vacuum permittivity, respectively. T is the thickness of the structure, that is, the same value for the fingers and the curved beams. When there is nonzero overlap between the fingers (C_A for $y_d \geqslant -l_{ol}$ and C_B for $y_d \leqslant l_{ol}$), the well-known parallel-plate capacitance formula was used. In addition, C_f was added to it, which represents the fringe capacitance, obtained from the COMSOL simulation results (Figure 3) at zero finger overlap. When there is no overlap between the fingers (C_A for $y_d < -l_{ol}$ and C_B for $y_d > l_{ol}$), the simulation results were numerically fitted (least-square algorithm) to an exponential decay function. a_0, a_1, a_2, b_1, and b_2 are the fitting parameters, which vary according to the geometries of the comb fingers. Figure 3 includes the plot (line) produced by using (5).

The governing equation of the whole system can be described as,

$$m\frac{\partial^2 y_d}{\partial t^2} + c_d\frac{\partial y_d}{\partial t} + F_r(y_d) - \frac{1}{2}\frac{\partial U_e}{\partial y_d} = F_{ext} = ma_{ext} \qquad (6)$$

$$U_e = \frac{1}{2}\left[C_A(V_S - V_A)^2 + C_B(V_S - V_B)^2\right] \qquad (7)$$

where c_d is a damping coefficient, U_e the electrostatic potential energy, and F_{ext} the external force (i.e., by vibration) exerted to the system. $F_r(y_d)$ is the restoring force of the curved beam, which can be expressed as:

$$F_r(y_d) = k_1 y_d + k_2 y_d^2 + k_3 y_d^3 \qquad (8)$$

where k_1, k_2, and k_3 denote the linear, quadratic, and cubic spring constants, respectively. A straight clamped-clamped beam results in k_1 and k_3 terms only while all of the terms are nonzero for a curved beam. The curve shape of the beam is designed to be that of the fundamental mode of the beam, which can be expressed as:

$$y_0(x) = \frac{h}{2}\left(1 - \cos\frac{2\pi x}{l}\right). \qquad (9)$$

The spring constants of the curved beam can be derived by using the Euler–Bernoulli theory of thin beams, Galerkin method (Lacarbonara et al., 1998), and single mode approximation. The overall derivation of the spring constants is described in detail by Casals-Terre et al. (2008), and only the results are repeated here:

$$k_1 = \frac{\pi^4 EwTN_s}{12l^3}\left(2w^2 + 3h^2\right) \qquad (10)$$

$$k_2 = \frac{3\pi^4 EwThN_s}{8l^3} \qquad (11)$$

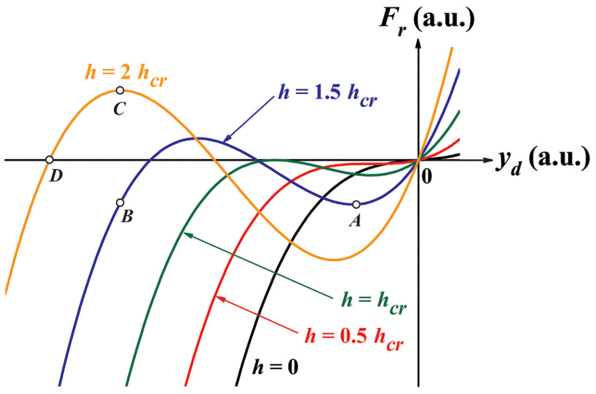

Figure 4. Exemplary plots of the restoring forces, $F_r(y_d)$, according to (8) for various beam height (h) values.

$$k_3 = \frac{\pi^4 EwTN_s}{8l^3} \tag{12}$$

where E and N_s are Young's modulus of the beam material, and a number of the springs, respectively.

Figure 4 presents an example of the restoring forces, $F_r(y_d)$, according to (8) and (10)–(12). For small magnitudes of displacement (y_d), the relationship is almost linear between F_r and y_d. As the magnitude of y_d increases, the nonlinearity becomes more notable. When h is larger than 0.5 h_{cr}, a negative slope starts to appear in the curves, which explains the snapping behavior of the curved beam—the beam is not stable within the region of a negative slope. As y_d reaches to the onset point of the negative slope (e.g., point A when $h = 1.5\ h_{cr}$), the beam snaps to the point of the same F_r value on the positive slope (i.e. point B). This snapping has an effect of increased movement and spectrum broadening. When h is between 0.5 h_{cr} and h_{cr}, however, the local maximum still has a negative value of F_r, and therefore, the beam goes back to the initial position when the external force is removed. In other words, it has only one stable idle position. When h is larger than h_{cr}, the local maximum becomes a positive value, and the beam has two stable idle positions. For example, when $h = 2\ h_{cr}$, the local maximum (point C) has a positive value of F_r, and the beam has a stable idle position at point D in addition to the origin. The higher order terms, the snapping behavior and the bistability, altogether, contribute to the nonlinear characteristics of the curved beams. On the other hand, as the beam height increases, the restoring force increases as well, which works against the beam displacement. Consequently, it can be surmised that there is an optimum value of the beam height that gives the maximum power output. This will be presented in more details in the results section. There is another nonlinearity coming from electrostatic component, making the overall problem complex. The present study approaches the problem with numerical analysis.

In order to solve the problem numerically, (2), (3), and (6) were modified into the following stochastic differential equations (SDE) (Ando et al., 2012):

$$dy_d = y_v dt \tag{13}$$

$$dy_v = -\frac{1}{m}\left[c_d y_v + F_r(y_d) - \frac{1}{2}\frac{dU_e}{y_v dt}\right]dt + \frac{\sigma}{m}dW_t = y_a dt \tag{14}$$

$$a_{ext} = \frac{\sigma}{m}\frac{dW_t}{dt} \tag{15}$$

$$dV_A = \frac{1}{C_A + C_p}\left[(V_S - V_A)dC_A - \frac{V_A}{R_{LA}}dt\right] \tag{16}$$

$$dV_B = \frac{1}{C_B + C_p}\left[(V_S - V_B)dC_B - \frac{V_B}{R_{LB}}dt\right] \tag{17}$$

where W_t denotes the Wiener process which models the stochastic vibration input. σ represents the diffusion coefficient that sets the input strength. y_v and y_a indicate velocity and acceleration of the mass, respectively. Euler–Maruyama method was used to solve the equations (Kloeden and Platen, 1995). As the Wiener process, a random uncorrelated time series with standard normal distribution (i.e., white noise) was generated in MATLAB®. The random series was, then, processed through a low pass filter to produce a colored noise signal. Considering the spectral features of various vibration energy sources that are available, the cutoff frequency of the low pass filter used in the input signal generation was set as 500 Hz in this study. To this noise, the diffusion coefficient (σ) was multiplied in order to set its strength. A time step of 50 ns was chosen in the simulation, which provided convergence.

The accuracy of the analysis improves according to the length of the input signal. There is a limit, however, due to the physical memory of the machine used for the analysis. Therefore, the calculation was repeated multiple times with a newly generated input signal for each round. The number of this repetition was determined by examining the distribution of the average of the input power spectral density, and their relative standard deviation between 0 and 300 Hz (Figure 5). It can be observed that the relative standard deviation decreases as the number of repeating signals increases. A time series with the length of forty million was generated for one signal, and signal generation was repeated for 500 times for one analysis. Overall, it is tantamount to a time series with the length of 20 billion. The time series of displacement, velocity, acceleration, charge, voltage, etc. were calculated by using (13)–(17), and the average power was calculated from them. Power spectral density was also calculated by using FFT (fast Fourier transform) function of the MATLAB®. Table 1 summarizes the values of the design parameters used in the analysis, which is based on the device reported by Honma et al. (2019). Single crystalline silicon (c-Si) was

Table 1. Nominal values of the design parameters used in the analysis.

Description (symbol)	Value	Description (symbol)	Value
Beam length (l)	8000 μm	Number of fingers (N_f)	900
Beam width (w)	20 μm	Finger gap (d_0)	9 μm
Structure thickness (T)	400 μm	Dielectric thickness (d_e)	0.85 μm
Number of hinges (N_s)	8	Relative permittivity of the dielectric (ε_e)	3.6
Young's modulus, c-Si (E)	179 GPa	Initial finger overlap (l_{ol})	150 μm
Proof mass (m)	2.5 g	Parasitic capacitance (C_p)	30 pF
Electret charging voltage (V_S)	200 V	Damping coefficient (c_d)	1 g/s

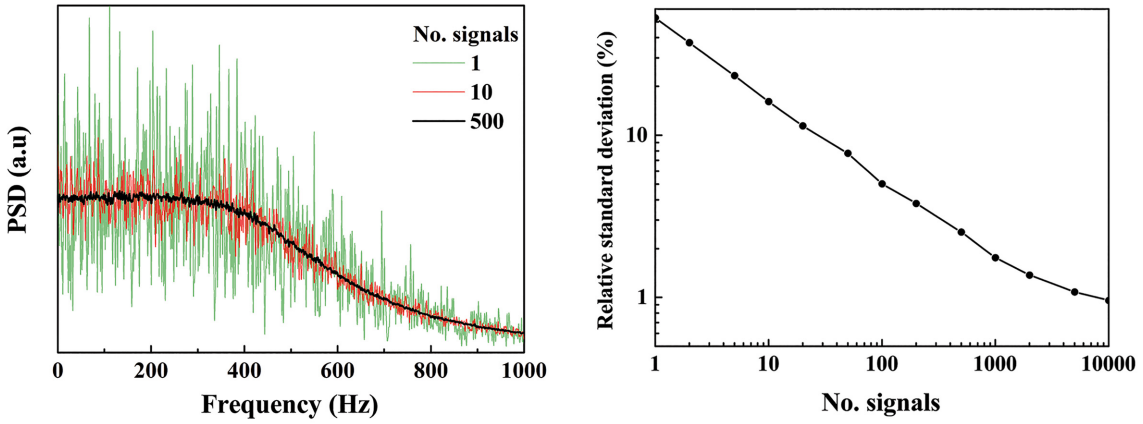

Figure 5. (a) Average power spectral density of input signal (F_{ext}) for different number of repeating signals. (b) Relative standard deviation of PSD under 300 Hz as a function of number of signals.

considered as the structural material, which is one of the most frequently used materials in microelectromechanical systems (MEMS).

Results

As the first step in the analysis, the developed model was examined with a sinusoidal vibration input, as it was the input condition used in the experiments of Honma et al. (2019). There were two aims in this step. The first aim was to verify the developed model by comparing it to the experimental results in the literature. With the similar device parameters, the calculated output power was about 1 mW, which is close to the value reported by Honma et al. (2019). The second aim was to determine the value of a damping coefficient, which also affects the power output and the spectral characteristics. The value was determined as 1 g/s, which falls within a reasonable range found from the devices in a similar scale (Lu et al., 2021; Zhou et al., 2014).

Figure 6 presents exemplary transient responses, including the external force (F_{ext}), the displacement of the moving part (y_d), and the produced electric current (i) passing through one of the loads. The rms magnitude of 0.01g was used as a_{ext}, where g is gravitational acceleration, 9.8 m/s^2. Similar signal patterns can be observed between the displacement and the current. Because of the balanced configuration, the electric power delivered to

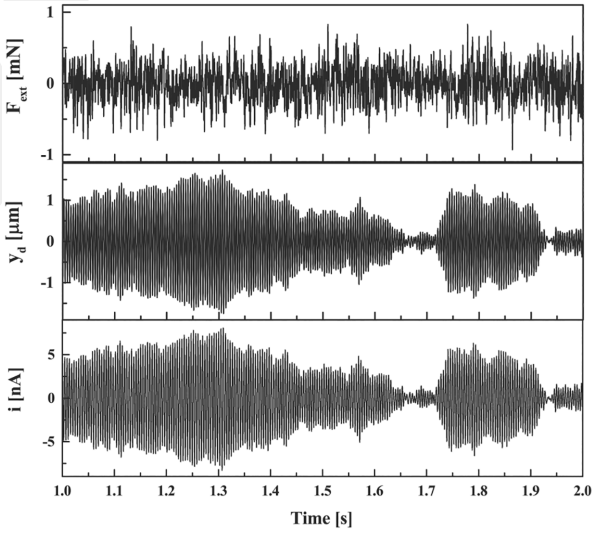

Figure 6. Example of signals for a duration of one second: (top) external force, (middle) displacement of the moving part, and (bottom) current through R_{LA}. h = 2 h_{cr}, a_{ext} (rms) = 0.01g, R_{LA} = R_{LB} = 200 MΩ.

the two loads are almost equal to each other in average. Exemplary phase portraits of the device are presented in Figure 7 when h = 2 h_{cr}. When the a_{ext} magnitude is small (0.02g), the displacement is also small, and the phase portrait remains around the origin (Figure 7(a)).

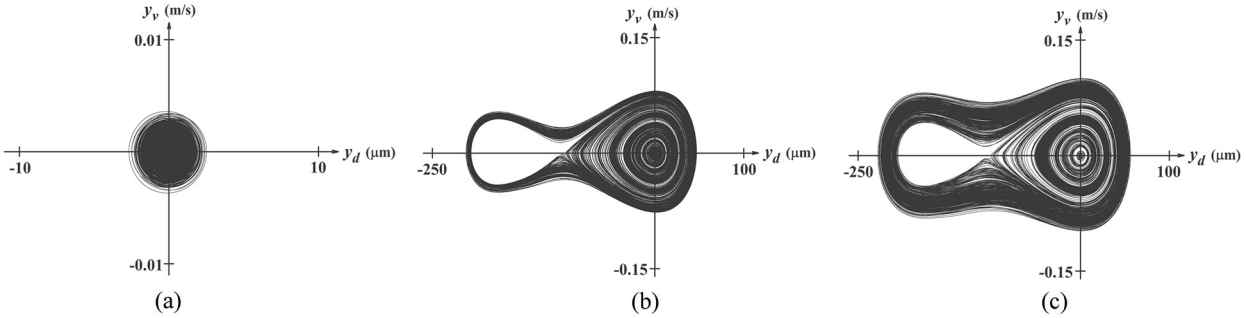

Figure 7. Phase portraits of the device in response to colored noise. h = 2 h_{cr} (92.4 μm), R_{LA} = R_{LB} = 30 MΩ. a_{ext} magnitudes (rms) are (a) 0.02 g, (b) 0.05 g, and (c) 0.1 g.

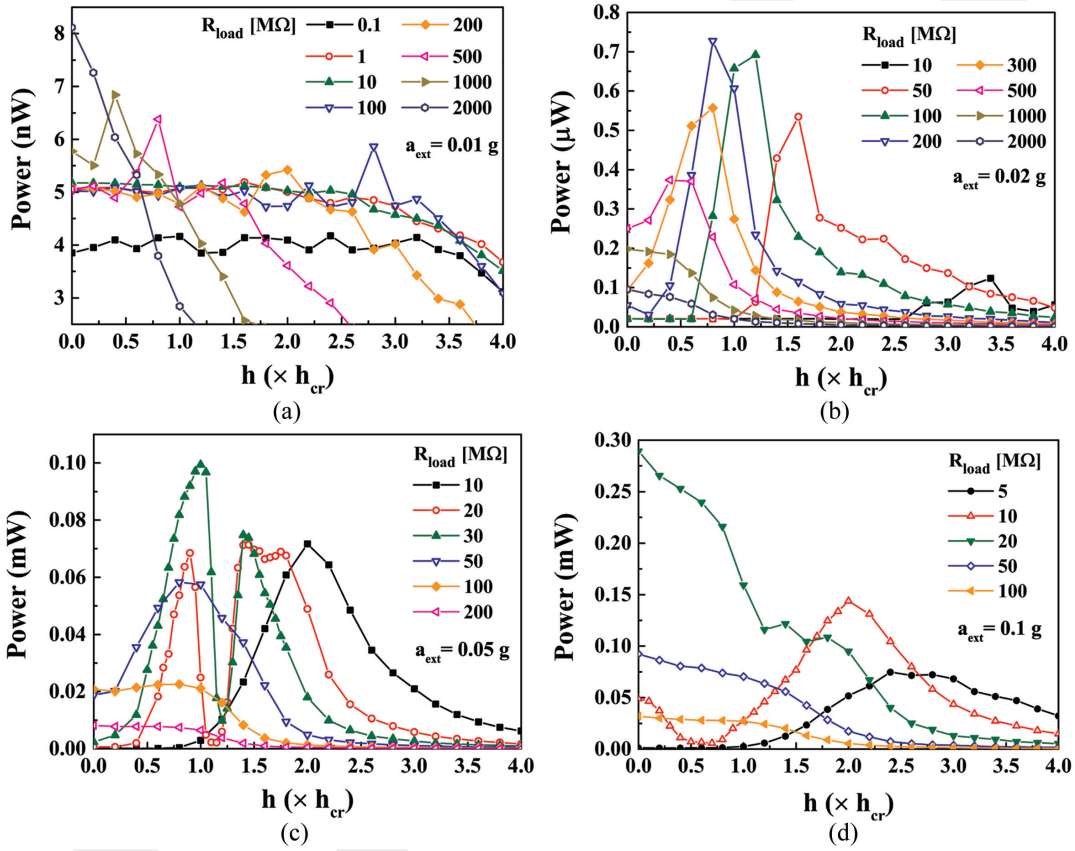

Figure 8. Calculated average electric power in response to colored noise, as a function of beam height h for various load conditions (R_{load} = R_{LA} = R_{LB}) when the exerted acceleration magnitudes (a_{ext}, rms) are (a) 0.01 g, (b) 0.02 g, (c) 0.05 g, and (d) 0.1 g. Beam heights are expressed with a unit of h_{cr}.

As the a_{ext} magnitude increases to 0.05g, leaping between the two stable points is observed (Figure 7(b)). When the a_{ext} magnitude increases further (0.1g), a substantial increase in the velocity can be observed while the displacement increases only slightly (Figure 7(c)).

Figure 8 shows the average electric power delivered to one of the loads for various a_{ext} magnitudes, load resistances, and beam heights. Based on the maximum power transfer theorem, an optimum load resistance value (R_{opt}) exists for each condition. For example, when a_{ext} is 0.02g (Figure 8(b)), the highest power is obtained with 200 MΩ. It is observed that the R_{opt} value decreases as a_{ext} increases. This could be understood in the following manner. As the displacement increases, the capacitance value changes more, which should be matched with a smaller value of resistance as the load.

Figure 8 also demonstrates that there is an optimum beam height (h_{opt}) for the maximum power output, which varies according to the input vibration strength. For the mid-range of the input acceleration, that is, when a_{ext} is 0.02g (Figure 8(b)) and 0.05g (Figure 8(c)), the curved beam produces higher power output than

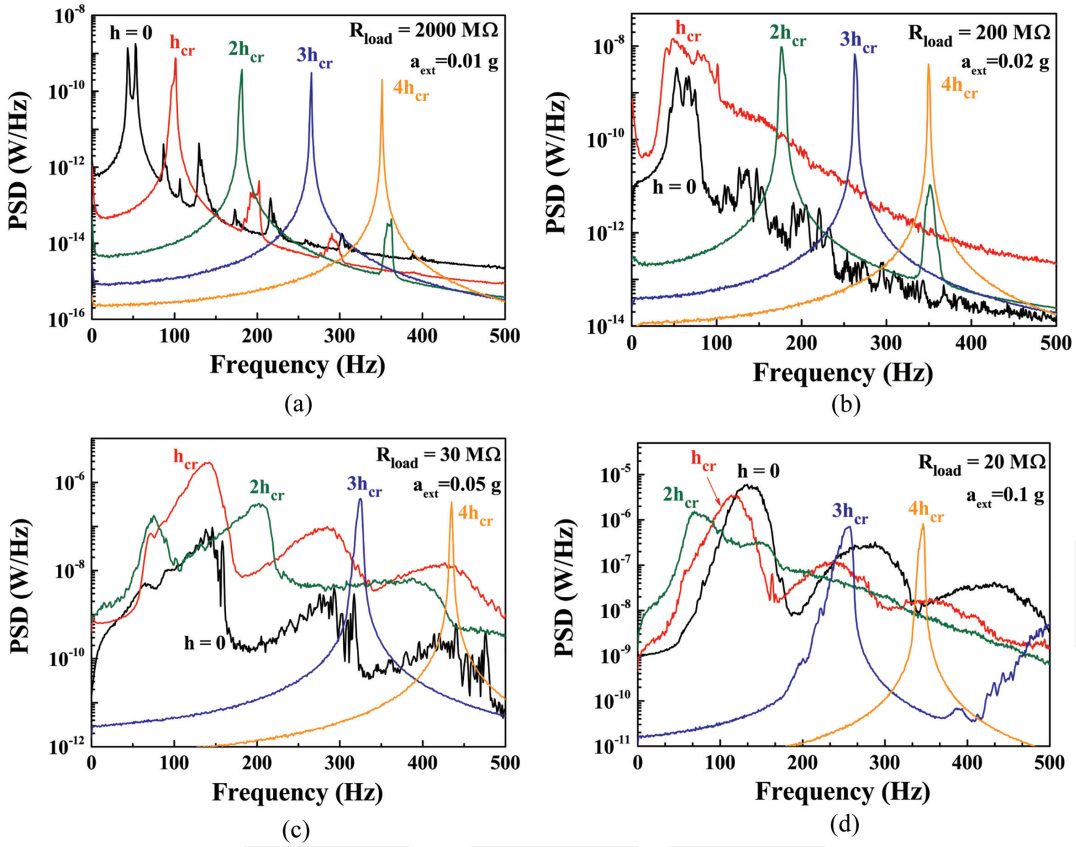

Figure 9. Calculated electric power spectral density (PSD) in response to colored noise, for various beam heights (h = 0, h_{cr}, 2 h_{cr}, …) when the exerted acceleration magnitudes (a_{ext}, rms) are (a) 0.01 g, (b) 0.02 g, (c) 0.05 g, and (d) 0.1 g. Load (R_{load}) conditions are those which give the highest overall power output for each input acceleration, in other words, R_{opt}.

the straight beam (h = 0), with h_{opt} being 0.8 h_{cr} and 1 h_{cr}, respectively. For a_{ext} of 0.02g, the curved beam with h = 0.8 h_{cr} produces 0.73 μW at R_{load} = 200 MΩ, which is 2.9 times higher than that of the straight beam (0.25 μW @ R_{load} = 500 MΩ). The improvement is higher when a_{ext} is 0.05g, where the curved beam with h = h_{cr} produces 99.4 μW at R_{load} = 30 MΩ, which is 4.8 times higher than that of the straight beam (20.8 μW @ R_{load} = 100 MΩ). To the contrary, for low and high magnitudes of the input acceleration, that is, when a_{ext} is 0.01g (Figure 8(a)) and 0.1g (Figure 8(d)), the straight beam produces the highest power output overall. Even though the curved beam produces higher power output than the straight beam at some load conditions, the global maximum is found with h = 0 for those input acceleration magnitudes. Consequently, it is necessary in practice to obtain the pre-knowledge of the characteristics of the vibration source in a specific application field, so that one can decide the optimum beam height accordingly.

The power versus beam height graphs show, in general, one of the following two trends: (1) increasing to reach a maximum power, then decreasing or (2) decreasing continuously. These trends are in accordance with the earlier description where it is explained that there are two effects at work with the beam height increase: (1) nonlinearity-induced enhancement and (2) increased spring constants. The case where the power continuously decreases according to h is when the latter effect is much more dominant than the former. In this regard, an interesting observation can be made when a_{ext} is 0.05g (Figure 8(c)), and R_{load} is 20 MΩ and 30 MΩ. For these cases, there are regions in the curves between 1 h_{cr} and 1.5 h_{cr} where the curves drop in the middle—in other words; two peaks are found in each curve. The reason behind this behavior is not clear yet, however, considered to be related to the effect of bistability.

The frequency characteristics of the VEH device were further examined with the electric power spectral densities (PSD) as shown in Figure 9. For these graphs, the loads are R_{opt}, which give the maximum overall power output for given conditions. When a_{ext} magnitude is 0.01g (Figure 9(a)), the PSD graphs resemble those of linear harmonic oscillators except for additional peaks resulting from nonlinearity, which appear especially in the devices with low h values. At a low vibration magnitude, the nonlinearity does not appear strongly for the curved beams. As the vibration magnitude increases (Figure 9(b) and (c)), broadening of the bandwidth can be observed, starting from the low beam heights. At the same time, one can

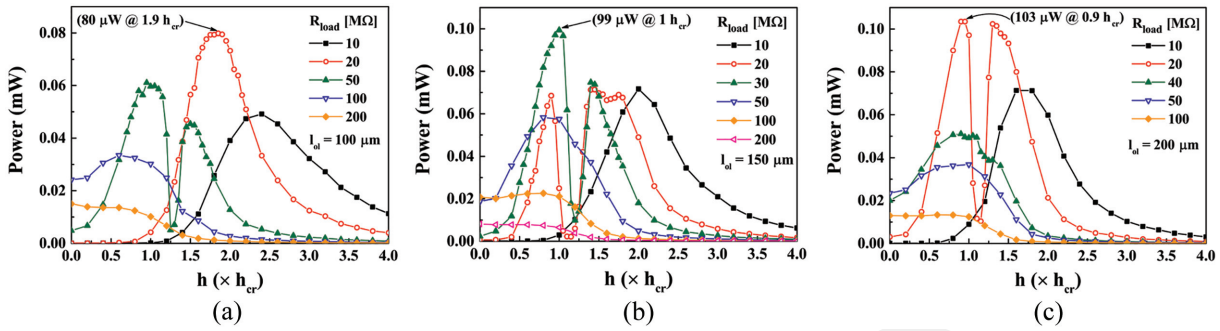

Figure 10. Effects of initial finger overlaps (l_{ol}) to the performances of VEHs. Calculated average electric power as a function of beam height h for various load conditions ($R_{load} = R_{LA} = R_{LB}$). l_{ol} is (a) 100 μm, (b) 150 μm, and (c) 200 μm. a_{ext} (rms) is 0.05g. For each value of l_{ol}, the maximum power and the optimum beam height (h_{opt}) are indicated in the plot.

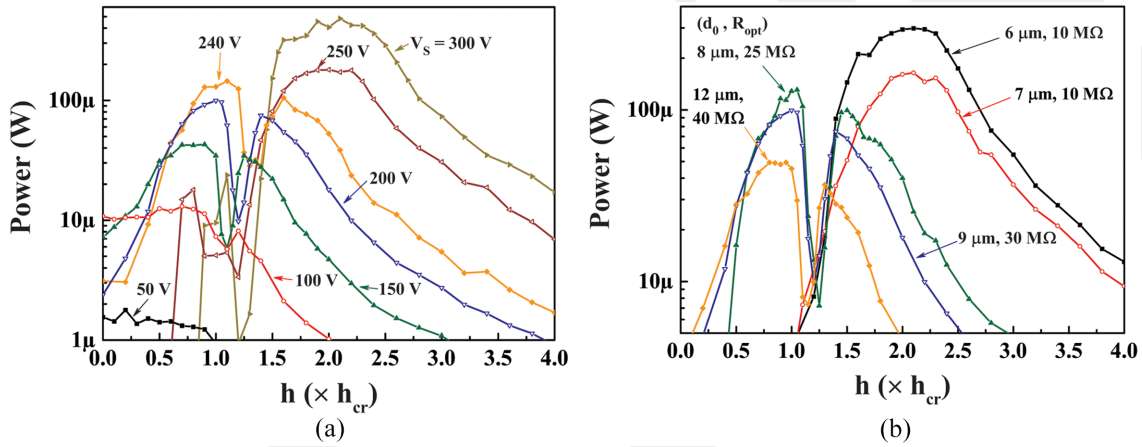

Figure 11. (a) Effects of surface potential (V_S) to the average electric power. d_0 = 9 μm. For V_S of 250 V and 300 V, R_{opt} is 15 MΩ. Otherwise, R_{opt} is 30 MΩ. (b) Effects of finger gap (d_0) to the average electric power. V_S = 200 V. For (a) and (b), a_{ext} (rms) is 0.05g.

observe that the straight beam also shows broadening in PSD. When the vibration magnitude is increased further (Figure 9(d)), the nonlinearity effect in the straight beam finally catches up, producing more power than the curved-beam devices owing to its lower spring constants. It is noteworthy to mention that these PSD graphs are different from those in response to ascending/descending frequency, which show hysteresis with spring hardening/softening characteristics because the frequency of the input changes in a random order in this analysis.

Finally, the effects of the electrical design parameters (initial finger overlap l_{ol}, surface potential V_S, and finger gap d_0) to the power output were examined. Figure 10 presents the effect of l_{ol}, which not only determines the capacitance values of the comb-drives, but also decides the displacement where the fingers start to be disengaged from each other. Three values of l_{ol} were included in the study: 100 μm (Figure 10(a)), 150 μm (nominal, Figure 10(b)) and 200 μm (Figure 10(c)). Only slight changes are observed when l_{ol} is increased from 150 μm to 200 μm. When l_{ol} is reduced to 100 μm, however, more significant changes are noticeable with the shift in the h_{opt} value and reduced maximum output power.

Figure 11(a) shows the effects of V_S. Only the graphs with the optimum load (R_{opt}) condition for each value of V_S are included in the plot. In the literature, the surface potentials are found to be, in general, between 100 and 300 V although a higher voltage (e.g., 500 V, Hagiwara et al., 2012) is also reported. The V_S values from 50 to 300 V were examined in this study. As V_S decreases from the nominal value (200 V), it can be observed that the maximum power output as well as the optimum beam height (h_{opt}) decrease. This trend can be understood from the fact that the amount of charges involved in the migration is proportional to the surface potential. Graphs at V_S = 50 V and 100 V show that at low V_S values, the benefit of the curved beams becomes significantly weaker. Up to 240 V of surface potential, the optimum load resistance (R_{opt}) is kept constant at 30 MΩ. When V_S becomes 250 V, several remarkable changes occur: (1) the maximum power output is found at the second peak, (2) h_{opt} becomes higher (around 2 h_{cr}), and (3) R_{opt} becomes smaller (15 MΩ instead of 30 MΩ). It can be surmised that at higher surface potential, the nonlinearity effects of the system become stronger. Figure 11(b) presents the effects of d_0. As the finger gap becomes narrower, h_{opt}

is shifted to the higher value, and R_{opt} becomes smaller. For d_0 value of 6 and 7 μm, the maximum power outputs are found at the second peak. These trends are found to be similar to those with respect to V_S, and can be understood in the same manner, that is, higher initial capacitance values lead to increased amount of charges involved in the migration ($Q = CV$). It should be noted that, however, further reduction of the finger gaps will make fabrication processes more challenging and may incur undesirable lateral pull-in behavior.

Conclusions

The effects of curved beam heights to the electric power produced by electret-based vibration energy harvesting devices have been examined via numerical analysis. Stochastic differential equations were used based on the colored noise input assumption. The established model was first verified by comparing the result to the reported ones available in the literature. It was learned that the effect of the beam height is heavily dependent on the strength of the vibration. At a low vibration magnitude ($a_{ext} = 0.01g$), a device with curved beams produced lower power output than a straight-beam device for given device geometries because it operates in the linear region with small displacement. With a mid-range-magnitude vibration, a device with curved beams produced significantly higher power output (4.8 times @ $0.05g$ and 2.9 times @ $0.02g$) than a straight-beam device. At higher vibration magnitude ($0.1g$), once again, a straight-beam device resulted in higher power output than a curved-beam device because the nonlinearity in straight beams becomes also strong, and because the straight beams are more compliant than the curved beams. This study shows that the type of the beam producing more power output as well as the optimum beam height highly depend on the characteristics of the external vibration (strength, spectrum, etc.), the device geometries, and the surface potential. Consequently, it is imperative to study the characteristics of the vibration sources beforehand, and to carry out a simulation study accordingly, in order to produce the most optimal device design for a specific application.

Declaration of conflicting interests

The author declared no potential conflicts of interest with respect to the research, authorship, and/or publication of this article.

Funding

The author received no financial support for the research, authorship, and/or publication of this article.

ORCID iD

Dooyoung Hah https://orcid.org/0000-0002-1290-0597

References

Ando B, Baglio S, Bulsara AR, et al. (2014) A bistable buckled beam based approach for vibrational energy harvesting. *Sensors and Actuators A: Physical* 211: 153–161.

Ando B, Baglio S, L'Episcopo G, et al. (2012) Investigation on mechanically bistable MEMS devices for energy harvesting from vibrations. *Journal of Microelectromechanical Systems* 21(4): 779–790.

Boland J, Chao YH, Suzuki Y, et al. (2003) Micro electret power generator. In: *Sixteenth annual international conference on micro electro mechanical systems, MEMS-03*, Kyoto, Japan, 23 January 2003, pp.538–541. New York: IEEE.

Casals-Terre J, Fargas-Marques A and Shkel AM (2008) Snap-action bistable micromechanisms actuated by nonlinear resonance. *Journal of Microelectromechanical Systems* 17(5): 1082–1093.

Cottone F, Gammaitoni L, Vocca H, et al. (2012) Piezoelectric buckled beams for random vibration energy harvesting. *Smart Materials and Structures* 21(3): 035021.

Cottone F, Vocca H and Gammaitoni L (2009) Nonlinear energy harvesting. *Physical Review Letters* 102: 080601.

De Paula AS, Inman DJ and Savi MA (2015) Energy harvesting in a nonlinear piezomagnetoelastic beam subjected to random excitation. *Mechanical Systems and Signal Processing* 54: 405–416.

Dhote S, Li H and Yang Z (2019) Multi-frequency responses of compliant orthoplanar spring designs for widening the bandwidth of piezoelectric energy harvesters. *International Journal of Mechanical Sciences* 157: 684–691.

Du H, Chau FS and Zhou G (2018) Harmonically-driven snapping of a micromachined bistable mechanism with ultra-small actuation stroke. *Journal of Microelectromechanical Systems* 27(1): 34–39.

Eltanany AM, Yoshimura T, Fujimura N, et al. (2017) Development of piezoelectric bistable energy harvester based on buckled beam with axially constrained end condition for human motion. *Japanese Journal of Applied Physics* 56(10S): 10PD02.

Erturk A, Hoffmann J and Inman DJ (2009) A piezomagnetoelastic structure for broadband vibration energy harvesting. *Applied Physics Letters* 94(25): 254102.

Ferrari M, Bau M, Guizzetti M, et al. (2011) A single-magnet nonlinear piezoelectric converter for enhanced energy harvesting from random vibrations. *Sensors and Actuators A: Physical* 172(1): 287–292.

Fu Q and Suzuki Y (2014) MEMS vibration electret energy harvester with combined electrodes. In: *27th Annual International Conference on Micro Electro Mechanical Systems, MEMS 2014*, San Francisco, CA, USA, 26–30 January 2014, pp.409–412. New York: IEEE.

Hagiwara K, Goto M, Iguchi Y, et al. (2012) Electret charging method based on soft X-ray photoionization for MEMS transducers. *IEEE Transactions on Dielectrics and Electrical Insulation* 19(4): 1291–1298.

Hah D (2021) Effects of curved-beam heights to harvested energy in a balanced comb-drive configuration. In: *2021 Symposium on design, test, integration & packaging of MEMS and MOEMS (DTIP)*, Paris, France, 25–27 August 2021. New York: IEEE.

Hajati A and Kim SG (2011) Ultra-wide bandwidth piezoelectric energy harvesting. *Applied Physics Letters* 99(8): 083105.

Honma H, Mitsuya H, Hashiguchi G, et al. (2018) Improvement of energy conversion effectiveness and maximum output power of electrostatic induction-type MEMS energy harvesters by using symmetric comb-electrode structures. *Journal of Micromechanics and Microengineering* 28(6): 064005.

Honma H, Tohyama Y and Toshiyoshi H (2019) A 1.3 milliwatts electrostatic vibrational energy harvester with minimal reactive power through reduced internal stray capacitances. In: *Transducers 2019 – Eurosensors XXXIII*, Berlin, Germany, 23–27 June 2019, pp.362–365. New York: IEEE.

Jang SJ, Rustighi E, Brennan MJ, et al. (2011) Design of a 2DOF vibrational energy harvesting device. *Journal of Intelligent Material Systems and Structures* 22(5): 443–448.

Kim IH, Jung HJ, Lee BM, et al. (2011) Broadband energy-harvesting using a two degree-of-freedom vibrating body. *Applied Physics Letters* 98(21): 214102.

Kloeden P and Platen E (1995) *Numerical Solution of Stochastic Differential Equations*. New York: Springer-Verlag.

Lacarbonara W, Nayfeh AH and Kreider W (1998) Experimental validation of reduction methods for nonlinear vibrations of distributed-parameter systems: Analysis of a buckled beam. *Nonlinear Dynamics* 17(2): 95–117.

Li X, Yu K, Upadrashta D, et al. (2019) Multi-branch sandwich piezoelectric energy harvester: Mathematical modeling and validation. *Smart Materials and Structures* 28(3): 035010.

Litak G, Friswell MI and Adhikari S (2010) Magnetopiezoelastic energy harvesting driven by random excitations. *Applied Physics Letters* 96(21): 214103.

Liu W, Formosa F, Badel A, et al. (2016) Investigation of a buckled beam generator with elastic clamp boundary. *Smart Materials and Structures* 25(11): 115045.

Lu Q, Fang W, Wang C, et al. (2021) Investigation of a complete squeeze-film damping model for MEMS devices. *Microsystems & Nanoengineering* 7: 54.

Meninger S, Mur-Miranda JO, Amirtharajah R, et al. (1999) Vibration-to-electric energy conversion. In: *Proceedings of the 1999 international symposium on Low power electronics and design*, San Diego, CA, USA, 16–17 August 1999, pp.48–53. New York: IEEE.

Nguyen SD and Halvorsen E (2011) Nonlinear springs for bandwidth-tolerant vibration energy harvesting. *Journal of Microelectromechanical Systems* 20(6): 1225–1227.

Nguyen SD, Halvorsen E and Paprotny I (2013) Bistable springs for wideband microelectromechanical energy harvesters. *Applied Physics Letters* 102(2): 023904.

Pereira TL, de Paula AS, Fabro AT, et al. (2019) Random effects in a nonlinear vibration-based piezoelectric energy harvesting system. *International Journal of Bifurcation and Chaos* 29(04): 1950046.

Qiu J, Lang JH and Slocum AH (2004) A curved-beam bistable mechanism. *Journal of Microelectromechanical Systems* 13(2): 137–146.

Roundy S, Wright PK and Rabaey J (2003) A study of low level vibrations as a power source for wireless sensor nodes. *Computer Communications* 26(11): 1131–1144.

Scerri J, Grech I, Gatt E, et al. (2015) Reduced-order model for MEMS PZT vibrational energy harvester exhibiting buckling bistability. *Electronics Letters* 51(5): 409–411.

Sebald G, Kuwano H, Guyomar D, et al. (2011) Experimental Duffing oscillator for broadband piezoelectric energy harvesting. *Smart Materials and Structures* 20(10): 102001.

Senturia SD (2007) *Microsystem Design*. New York: Springer Science & Business Media.

Sterken T, Baert K, Puers R, et al. (2003) A new power MEMS component with variable capacitance. In: *Pan Pacific Mircoelectronics Symposium*, Island of Hawaii, HI, USA, 18–20 February 2003, pp.27–34. Eden Prairie: Surface Mount Technology Association.

Tang L and Yang Y (2012) A multiple-degree-of-freedom piezoelectric energy harvesting model. *Journal of Intelligent Material Systems and Structures* 23(14): 1631–1647.

Torres EO and Rincon-Mora GA (2006) Electrostatic energy harvester and Li-ion charger circuit for micro-scale applications. In: *49th IEEE International Midwest Symposium on Circuits and Systems*, San Juan, PR, USA, 6–9 August 2006, pp.65–69. New York: IEEE

Upadrashta D and Yang Y (2018) Trident-shaped multimodal piezoelectric energy harvester. *Journal of Aerospace Engineering* 31(5): 04018070.

Van Blarigan L, Danzl P and Moehlis J (2012) A broadband vibrational energy harvester. *Applied Physics Letters* 100(25): 253904.

Wu H, Tang L, Yang Y, et al (2013) A novel two-degrees-of-freedom piezoelectric energy harvester. *Journal of Intelligent Material Systems and Structures* 24(3): 357–368.

Xiao Z, Yang TQ, Dong Y, et al. (2014) Energy harvester array using piezoelectric circular diaphragm for broadband vibration. *Applied Physics Letters* 104(22): 223904.

Xue H, Hu Y and Wang QM (2008) Broadband piezoelectric energy harvesting devices using multiple bimorphs with different operating frequencies. *IEEE Transactions on Ultrasonics, Ferroelectrics, and Frequency Control* 55(9): 2104–2108.

Yang Z, Tang L, Tao K, et al. (2019) Modelling and validation of electret–based vibration energy harvesters in view of charge migration. *International Journal of Precision Engineering and Manufacturing-Green Technology* 8(1): 113–123.

Zhang Y, Wang T, Luo A, et al. (2018) Micro electrostatic energy harvester with both broad bandwidth and high normalized power density. *Applied Energy* 212: 362–371.

Zhao S and Erturk A (2012) Electroelastic modeling and experimental validations of piezoelectric energy harvesting from broadband random vibrations of cantilevered bimorphs. *Smart Materials and Structures* 22(1): 015002.

Zhou W, Chen Y, Peng B, et al. (2014) Air damping analysis in comb microaccelerometer. *Advances in Mechanical Engineering* 6: 373172.

Zhu Y and Zu JW (2013) Enhanced buckled-beam piezoelectric energy harvesting using midpoint magnetic force. *Applied Physics Letters* 103(4): 041905.